

Modeling Electromagnetic Signal Injection Attacks on Camera-based Smart Systems: Applications and Mitigation

Youqian Zhang, Michael Cheung, Chunxi Yang, Xinwei Zhai, Zitong Shen, Xinyu Ji,
Eugene Y. Fu, Sze-Yiu Chau, Xiapu Luo

Abstract—Numerous safety- or security-critical systems depend on cameras to perceive their surroundings, further allowing artificial intelligence (AI) to analyze the captured images to make important decisions. However, a concerning attack vector has emerged, namely, electromagnetic waves, which pose a threat to the integrity of these systems. Such attacks enable attackers to manipulate the images remotely, leading to incorrect AI decisions, e.g., autonomous vehicles missing detecting obstacles ahead resulting in collisions. The lack of understanding regarding how different systems react to such attacks poses a significant security risk. Furthermore, no effective solutions have been demonstrated to mitigate this threat.

To address these gaps, we modeled the attacks and developed a simulation method for generating adversarial images. Through rigorous analysis, we confirmed that the effects of the simulated adversarial images are indistinguishable from those from real attacks. This method enables researchers and engineers to rapidly assess the susceptibility of various AI vision applications to these attacks, without the need for constructing complicated attack devices. In our experiments, most of the models demonstrated vulnerabilities to these attacks, emphasizing the need to enhance their robustness. Fortunately, our modeling and simulation method serves as a stepping stone toward developing more resilient models. We present a pilot study on adversarial training to improve their robustness against attacks, and our results demonstrate a significant improvement by recovering up to 91% performance, offering a promising direction for mitigating this threat.

I. INTRODUCTION

The rapid advancement of artificial intelligence (AI) has transformed numerous devices and applications into intelligent systems. These systems can perceive and interact with the physical world, as they are integrated with various sensors. Cameras are one of the pivotal components in many safety- and security-critical systems such as surveillance, autonomous vehicles, and industrial quality control, where image data are processed to make critical decisions. For example, smart security cameras can identify anomalies and activate alarms, autonomous vehicles can detect obstacles to prevent accidents, and AI-powered visual inspection systems can identify product defects.

For these camera-based smart systems to function reliably, the integrity of captured images is crucial. While digital

adversarial attacks have received significant attention, where attackers can modify input images at a pixel level, there is a growing interest in physical adversarial attacks, which involve malicious manipulations in the physical space [1]. For example, attackers employ various techniques to deceive/fool AI models (e.g., misclassification) such as carefully designed adversarial patches or stickers on the surface of objects, camouflage methods to modify object appearance and make them blend with the surroundings, and projecting arbitrary light onto objects [1]. Beyond these attacks targeting the objects, recent research has discovered various attack vectors to maliciously interfere with the cameras, for example, pointing lasers/lights at the lenses to blind cameras [2]–[8], broadcasting ultrasounds to pervert camera stabilizers resulting image blurring [9]–[11], and radiating electromagnetic waves to disturb image transmissions leading to color distortion in images [12]–[14]. It has been demonstrated that such external interference with cameras can cause performance degradation of image-related tasks, and a detailed discussion is presented in Section VIII.

Our focus of this work is on the lately proposed and demonstrated attacks using electromagnetic waves [12], [14]. We denote the attacks as *electromagnetic signal injection attacks* in this work. Such attacks aim to disrupt electrical signals in circuits by injecting electromagnetic signals, and as such cause visual distortions like purple stripes in images (as shown in Figure 1), ultimately leading to incorrect decisions made by the system. For instance, as depicted in Figure 1, attackers could conduct the attacks onto an autonomous car and alter the captured images (or frames) so as to hide a motorcycle, potentially causing the car to miss it and leading to a serious accident. It is essential to point out that electromagnetic signal injection attacks could be more accessible to an attacker for wide abuse as they do not require light-of-sight and precise timing control, unlike lasers and ultrasounds that need to be precisely directed to the cameras [14].

As mentioned previously, there are many different camera-based smart systems, and yet, the impacts of such attacks on these systems are not fully understood. Due to the complexity involved in building attack devices and conducting practical attacks, it remains challenging for researchers or engineers to test and determine the robustness of their models/systems against such attacks; in addition, it is also arduous to collect images under attacks, and harder to develop defenses to mitigate the attacks. To overcome these challenges, we are motivated to propose and develop a method that can generate

The authors are affiliated with The Hong Kong Polytechnic University, except that Sze-Yiu Chau is affiliated with The Chinese University of Hong Kong. The contacts are {you-qian.zhang}, {mkmcheun}, {chunxi.yang}, {xinwei.zhai}, {xinyu.ji}, {eugene.fu}, {daniel.xiapu.luo}@polyu.edu.hk, zitong.shen@connect.polyu.hk, sychau@ie.cuhk.edu.hk

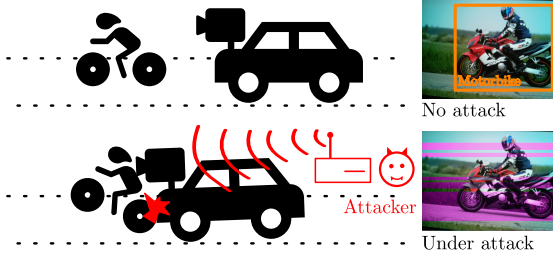


Fig. 1. When no attack exists, the autonomous car can accurately detect a motorcycle in the captured image. However, when under attack, the image is manipulated to display purple strips that mask obstacles, tricking the car into believing the road ahead is clear, possibly leading to a crash.

arbitrarily manipulated images, which can facilitate robustness testing and defense development.

In this work, we will propose a generalized model for different systems and present a simulation method that mimics the real-world attack process, ensuring that the simulated adversarial pattern closely resembles those affected by the actual attacks. It is essential to point out that the modeling and the simulation are not as straightforward as they might sound. Firstly, real-world attacks involve intricate interactions between electromagnetic waves, camera circuits, and the specific image formation process; accurately replicating these interactions is rather complex. Secondly, the exact parameters of an effective attack, such as the frequency, strength, and waveform of the electromagnetic signal, might be various, when considering the attacker's goals and resources. This makes it difficult to capture the full range of potential attack scenarios. To address these challenges, we abstract high-level models from practice, incorporating and unifying system varieties, and also, attackers' capabilities and limitations. These models will allow us to focus on evaluating the impacts of the attacks on images without being bothered by specific attack details, and further clarifying the principles of the simulation method.

In terms of the simulated adversarial pattern, a critical question arises: How similar are they to those under real-world attacks? To answer this question, we will build an attack setup and collect real-world data. Then, we will evaluate the similarity between simulated and real-world adversarial images systematically, and show that they are consistent regarding multiple aspects.

By utilizing this simulation method, we will demonstrate in a case study that many camera-based smart applications are susceptible to electromagnetic signal injection attacks. This raises another crucial question: How can the system under attack be effectively protected from the attacks? Some defenses have been proposed and discussed, but they come with certain limitations. For instance, conventional methods like incorporating additional electromagnetic shielding materials can significantly reduce the impact of external electromagnetic waves. Implementing this solution is challenging in weight- or size-restricted applications such as implantable medical devices or aviation; any unavoidable holes, such as

apertures in a shielded enclosure for optical display [15] or cable penetrations [16], may lead to degradation of shielding performance. Jiang et al., [12] proposed a specific detection method that involves modifying protocols to handle disrupted data packets (which are impacted by the attacks), allowing the system to know the existence of the attacks. Yet, a method that can properly mitigate the impacts caused by the attacks has not been presented. To bridge this gap, we present a case study of adversarial training that enhances the robustness of models against the attacks, thereby mitigating the negative consequences.

The contributions of this work are summarized as follows:

- **Modeling:** By proposing a generalized system model, we unify and simplify complex attack patterns observed across different applications. This will expedite the vulnerability evaluation process for researchers or practitioners. (Section III).
- **Simulation:** We develop a simulation method for generating adversarial images. Unlike traditional methods that rely on physical attacks in controlled environments, our approach offers an efficient and controllable way to evaluate the impact of the attacks on various applications. (Section IV)
- **High Similarity:** A rigorous evaluation is conducted to demonstrate that the simulated adversarial pattern achieves high similarity to real-world attacks. (Section V)
- **Vulnerability Expansion:** We employ the simulation method to identify a broader range of computer vision applications susceptible to the attacks, expanding the scope of concern beyond previously studied areas. (Section VI-A)
- **Robustness Enhancement:** We present fine-tuning models with the simulated adversarial images that can enhance the robustness of models against electromagnetic signal injection attacks. This approach can demonstrably recover up to 91% of the performance, highlighting its effectiveness in mitigating the threat. (Section VI-B)

II. BACKGROUND

This section delves into electromagnetic signal injection attacks by examining how they exploit vulnerabilities at the circuit level, and next, it briefly introduces some crucial applications of camera-based smart systems.

A. Electromagnetic Signal Injection Attacks

Within electronic devices, cables (or traces) act as communication pathways, connecting different components. These cables, essentially made of conductive metals like copper, possess inherent antenna-like properties, meaning that they can capture electromagnetic waves from their surroundings [17], [18]. Such antenna-like behavior creates an attack surface where attackers can inject electromagnetic signals. The injected signals will be superimposed with original signals that are transmitted in the cables, changing signal waveforms, as shown in Figure 2 for instance. Research suggests that the effectiveness and the efficiency of the injection are primarily influenced by two key variables: attack power and attack

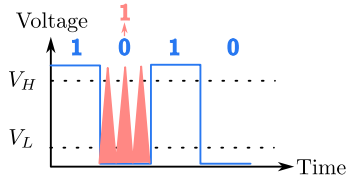


Fig. 2. A 0 is incorrectly detected as a 1. A malicious electromagnetic signal (red) is superimposed with the original signal (blue), causing the voltage level higher than the threshold V_H of the receiving circuit, and leading to 1 detected.

frequency [19]. Regarding the attack power, a strong enough injected signal is crucial for causing a significant impact, where increasing the power level enhances the likelihood of successful manipulation [20]. In terms of the attack frequency, the injected signal's frequency needs to be the same as the cable's resonant frequency to maximize the injected power [21].

Following the injection, the circuit's response to the manipulated signal determines the attack's success. Note that this work focuses specifically on how the electromagnetic signal injection attacks affect digital signals, represented by binary sequences of 0s and 1s. Receiving circuits rely on voltage thresholds to differentiate between 0 and 1. As illustrated in Figure 2, voltages lower than a lower threshold V_L correspond to 0s, and voltages higher than a higher threshold V_H correspond to 1s. As mentioned earlier, injected signals can alter the signal waveform. This manipulation can push the voltage level representing a 0 up to a level interpreted as a 1, or vice versa, leading to incorrect reception. This principle has been validated in numerous studies [12], [20], [22]–[28]. In simpler terms, the attacks can cause errors in data transmission by flipping bits.

B. Camera-based Smart Applications

Cameras equip computers/machines with the capability to perceive the environment, and computer vision algorithms [29] provide intelligence that enables automatic extraction, analysis, and understanding of useful information from a single image or a sequence of images. There are many different applications, and this work focuses on the following widely used categories [29]–[31], which will be critically discussed and evaluated in our work.

Image classification is a fundamental application that involves assigning categories or labels to images based on their visual content. It enables machines to recognize and categorize objects, scenes, or patterns within images.

Object detection enables identifying and localizing objects within an image. It goes beyond image classification by not only determining the presence of objects but also providing their precise spatial location. This task is valuable in various applications, including autonomous driving, surveillance, and object tracking.

Instance segmentation is a more advanced application that aims to identify and delineate individual instances of objects within an image with pixel-level accuracy. It combines the capabilities of both object detection and semantic segmentation, providing detailed information about the object boundaries.

Instance segmentation is valuable in scenarios where precise object separation is required, such as in medical imaging, robotics, and video analysis.

Face recognition is a specialized technique that focuses on identifying individuals from images or video frames based on their facial features and characteristics. It involves capturing and analyzing facial patterns, such as the arrangement of the coordinates of eyes, nose, and mouth, to establish a unique identity. Face recognition has applications in various domains, including security systems, biometric identification, and human-computer interaction.

Depth estimation is the application of determining the distance or depth of objects within an image. It enables machines to perceive the three-dimensional structure of a scene, which is crucial for tasks such as scene reconstruction, augmented reality, and robot navigation.

III. MODELING AND ATTACK PRINCIPLE

This section begins by abstracting a high-level system model commonly found in different camera-based smart systems, and also, presenting an attacker model, stating their capabilities and limitations. Based on the models, we further elaborate the attack principles.

A. System Model

A camera-based smart system, as depicted in Figure 3, consists of two components: an image sensor and a processing unit. The image sensor captures visual information from the physical world, while the processing unit analyzes the captured information.

The image sensor is used to convert light into electrical signals – it's made up of millions of light detectors called photodiodes, and each is sensitive to light and generates an electrical current proportional to the light intensity it receives. To capture color information, a color filter array (CFA) is placed over the photodiodes. Each filter within the CFA only allows light with a specific color to reach the underlying photodiode. Note that each photodiode corresponds to a pixel, and all pixels form a raw image, denoted as I , where each pixel location only holds information for a single color channel. One of the commonly used CFAs is the Bayer filter array [32], and an example is shown in Figure 3. The pattern alternates blue and red filters in the horizontal and vertical directions, and green filters organized in the quincunx pattern at the remaining locations [33]. The red, green, and blue pixels are denoted as R, G, and B accordingly, and the arrays of these pixels form the raw image.

The raw image is then transmitted from the sensor to the processing unit via a cable. The transmission happens row by row, with each row packaged as a data packet. Note that if a data packet is corrupted, the processing unit will directly drop that packet and replace the missing one with the subsequent packet [12]. Upon receiving the raw image, the processing unit first performs "Image Reconstruction" as shown in Figure 3. One crucial step in the image reconstruction is demosaicing, which estimates the missing color information for each pixel by analyzing the colors of neighboring pixels. Taking

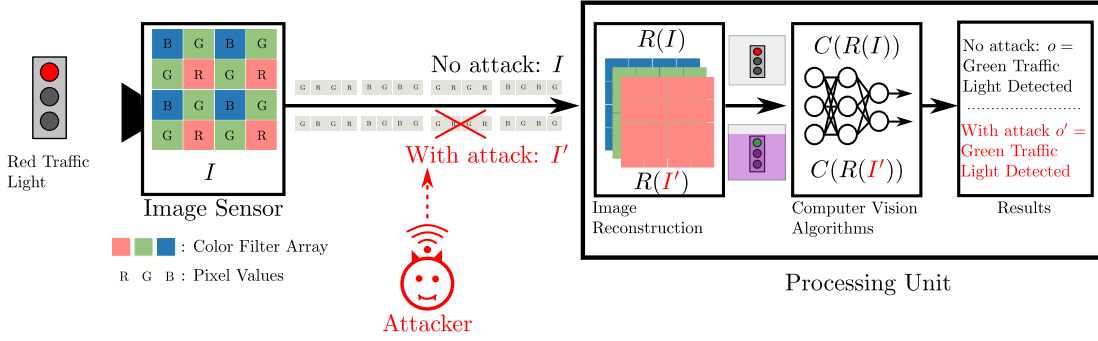


Fig. 3. A camera-based smart system consists of an image sensor and a processing unit, which can capture images and process the information, respectively. When no attack happens, the processing unit can give correct results, but an attack can cause a wrong result.

the images shown in Figure 3 as an example, this process transforms the raw image into a full-color representation with red, green, and blue values for each pixel, creating a complete image. Additionally, the image reconstruction block might apply further enhancements such as noise reduction and white balancing to improve the image quality. We combined all these essential reconstruction processes into a function $R(\cdot)$, and thus, $R(I)$ represents the reconstructed image.

Once the image is reconstructed, the processing unit can perform “Computer Vision Algorithms”, handling diverse functionalities like object detection, image segmentation, facial recognition, etc. We use a function $C(\cdot)$ to denote these algorithms. The final output of the camera-based smart system, denoted as o , represents the results of these algorithms. The equation below summarizes the operation of the system:

$$o = C(R(I))$$

B. Attacker Model

The attacker’s objective is to cause the computer vision algorithm to make wrong decisions by using electromagnetic waves to interfere with the raw image. We represent such a raw image under the attack as I' . We considered an attacker with no physical access to the system, and the attacker cannot tamper with the image reconstruction function $R(\cdot)$ or the computer vision algorithms $C(\cdot)$. The attacker possesses specialized equipment capable of generating arbitrary electromagnetic waves, meaning that the waveforms can be fine-tuned so as to achieve effective and efficient attacks (see detailed explanation in Section II-A). The attacker radiates the adversarial electromagnetic waves by antennas and injects them into the system. In addition, the attacker can obtain the timing information about when an image is being transmitted. For example, this can be done by capturing electromagnetic emanations from the system, and by analyzing these emissions, they can potentially extract timing information [12], [34]. The timing information allows the attacker to selectively target specific data packets for manipulation.

C. Attack Principle

Recall that a cable is used to connect the image sensor and the processing unit. As discussed in Section II, this cable presents a potential attack surface: while designed for

data transmission, it also acts as an antenna, susceptible to external electromagnetic interference. The attacker can exploit this antenna property by injecting arbitrary electromagnetic waves into the cable, causing bit flips and corrupting the data packet transmission between the image sensor and the processing unit. As mentioned in the system model, the corrupted packet is discarded and the missing information is replaced by the subsequent packet. Such a replacement will further disrupt the demosaicing process, leading to color strips in the reconstructed image.

Figure 4 illustrates how the color strips appear in an image. Let’s assume an attack causes the loss of the 1st row in the “Raw Image I ”, which contains green (G) values and red (R) values, i.e., GRGR. The processing unit fills the gap using information from the 2nd row of pixels, i.e., BGBG. This can result in incorrect color replacements during demosaicing because, as shown in “Raw Image under Attack I' ”, missing green values (G) are replaced with blue (B) and red (R) with green (G). Similarly, in the 2nd row, its values are replaced by the 3rd row, thus blue (B) replaced with green (G), and green (G) replaced with red (R). Such an incorrect color transformation will continue until another row of pixels is lost, for example, when the 4th row is lost. As a result, a color strip is formed by causing two rows of pixels to drop in the reconstructed image. With more rows being dropped, more strips appear. As shown in Figure 5, (b), i.e., I' , with multiple dropped rows may not look too much different from (a), i.e., I . However, after the reconstruction, multiple color strips appear in the image (c), i.e., $R(I')$.

IV. SIMULATION METHOD

In this section, we introduce how to simulate adversarial color strips that can resemble real attacks’ impacts.

A. Characterizing Color Strips

To simulate the attack effects, it’s essential to identify the rows of pixels targeted for removal, which mimics data loss during transmission caused by the attack. The selection strategy for these rows depends on the desired impact on the image, such as introducing specific color strips to disrupt key image features. This work focuses on a general simulation approach, leaving the specific row selection method open for customization based on the application.

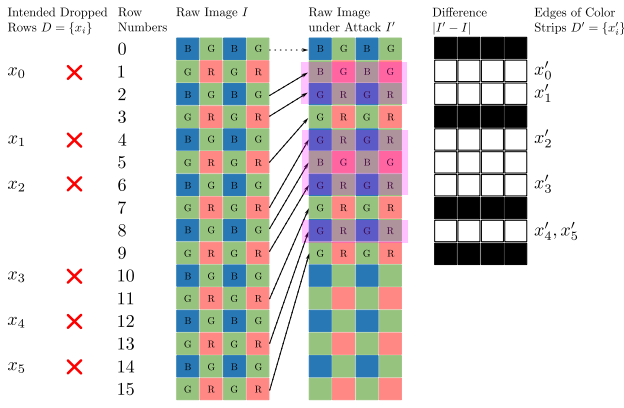


Fig. 4. Rows are dropped from a raw image I , leading to the raw image under the attack I' . The empty places in I' will be filled by pixels from the next frame.

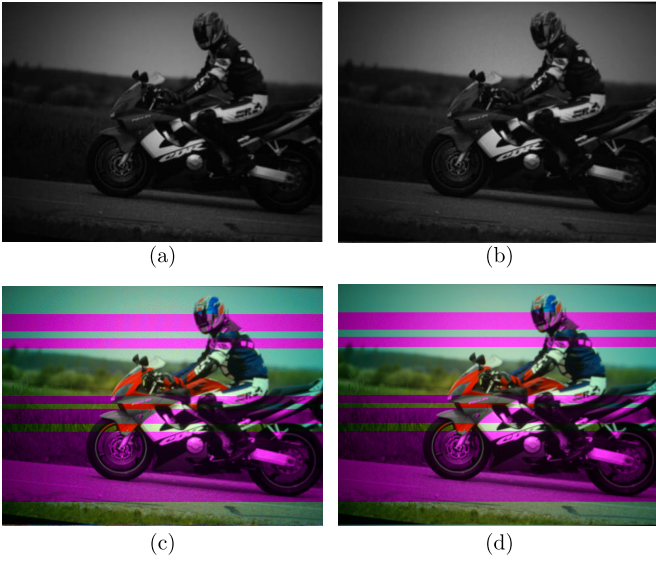


Fig. 5. (a) is the raw image without attack, i.e., I . (b) is the raw image under attack I' . (c) is the reconstructed image of the raw image under attack $R(I')$, showing multiple purple strips. (d) is the simulated adversarial image $R(I^s)$, which replicates the color strips the same as (c).

We define a set D including m distinct indices of intended dropped rows for I , and the elements in D are arranged in an ascending order:

$$D = [x_0, x_1, \dots, x_{m-1}]$$

As discussed previously, a color strip is paired up with two dropped rows, and hence, the total number of strips is $n = \lceil \frac{m}{2} \rceil$. Note that if two consecutive rows are dropped, there will not cause any incorrect color transformation. Since this work focuses on simulating color strips, and dropping rows consecutively is not considered in this work.

Regarding the positions of the color strips in an image, as demonstrated in Figure 4, the 0^{th} strip starts at x'_0 and ends at x'_1 , and the 1^{st} strip from x'_2 to x'_3 , and so on. In general, a color strip starts at x'_i , where i is an even number, and ends at x'_{i+1} . The height of the strip is $x'_{i+1} - x'_i + 1$, while the width of the strip is constant, which is the same as the width of the image. It is essential to note that a special case is when

Algorithm 1: Simulation Method

input : A raw image I , a set D of indices of rows to be dropped

output: A raw image I^s under simulated attack impacts.

- 1 $D \leftarrow \text{DescendingSort}(D)$ // Sort dropped indices in a descending order.
- 2 **for** x_i **in** D **do**
- 3 $I \leftarrow \text{Append}(I[0 : x_i - 1, :], I[x_i + 1 :, :])$
 // drop x_i -th row.
- 4 **end**
- 5 $I^s \leftarrow P(I, m)$ // Padding.

$i = m - 1$ is even, and the strip will start from x'_{m-1} until the end of the image.

From Figure 4, it is not difficult to observe that $x_i \neq x'_i, i \in \mathbb{Z}^+$, while $x_0 = x'_0$. We can deduce the relationship between x_i and x'_i so as to know where the strips will appear:

$$x'_i = \begin{cases} x_i, & \text{if } i = 0 \\ x_i - 2 \times \lfloor \frac{i+1}{2} \rfloor, & \text{otherwise} \end{cases} \quad (1)$$

While removing rows reduces image height by m , the processing unit will maintain the original dimensions for easier processing and analysis. As explained in our system model, this is achieved through padding, and for generality, we define the padding process as a function $P(I, m)$, meaning padding m rows to the bottom of I . For example, one approach involves appending the first m rows of the original data to the bottom of the manipulated image. This simulates the scenario where the attack causes data from subsequent frames to shift upwards, filling the gap created by the dropped rows.

The simulation process is summarized in Algorithm 1. It first sorts the dropped row indices in descending order allowing the removal to happen from the bottom upwards. The loop iterates through each dropped row index and removes the corresponding row in a raw image. Finally, the manipulated data is obtained by padding missing rows. We denote the simulated adversarial image as I^s , and the reconstructed image that will be further processed by computer vision algorithms is $R(I^s)$.

B. Data Collection

Since there is no open-source image dataset essential for our simulation and evaluation purposes, we built an experimental setup to collect data. The experimental setup used for demonstrating the attacks and data collection is depicted in Figure 6.

We used a computer to display open-source images on a 4K monitor. Besides, we randomly selected 100 photos from the COCO2017 testing dataset [35].

The components at the center of Figure 6 are utilized to capture raw images of the content displayed on the 4K monitor. A cable is employed to connect the image sensor to a Raspberry Pi, which serves as the storage device for the raw images. It should be noted that the raw images are subsequently transmitted to the computer for further processing.

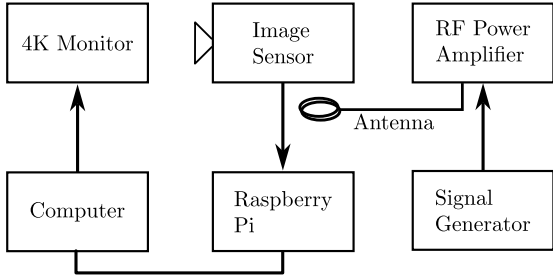


Fig. 6. The experimental setup employed for data collection. A 4K monitor is utilized to display open-source images, while an image sensor connected to a Raspberry Pi captures the raw images. The attacking signal is generated by a signal generator, amplified by the RF Power amplifier, and then radiated through an antenna.

Regarding the attack setup, a signal generator has been employed to create the desired attacking signal. The generated attacking signal is then amplified in signal strength using a radio-frequency (RF) power amplifier. An antenna is positioned around the cable that connects the image sensor and the Raspberry Pi, enabling wireless transmission of the attacking signal and aiming to inject and disrupt the data transmission between these components.

During the data collection process, we followed a specific procedure for each picture displayed on the monitor. First, we captured two consecutive raw images (I) in the absence of any attacks. Next, we adjusted the frequency and power of the attacking signals to generate an average occurrence of 3 strips within a raw image (I'). This process was then repeated, fine-tuning the attacking signals to achieve 6, and 15 strips, respectively.

C. Identifying Dropped Rows

In order to simulate the color strips the same as I' , it is necessary to know which rows are dropped in practical attacks, i.e., finding D . This is challenging as the camera-based smart systems do not provide the information about the dropped rows to users. We develop the following tricky method to obtain it, regardless of the types of camera-based smart systems.

Recall that the two images I' and I are supposed to be the same except for the dropped rows. Although noise also causes difference, since the noise is too small to cause significant impacts, the difference between the images can be simplified as being caused by the dropped rows. As shown in Figure 4, we subtract I' from I , and keep the absolute values, i.e., $|I - I'|$, and the smaller (larger) the difference, the darker (brighter) the pixel. Before the 0^{th} dropped row (i.e., x_0), rows in I' and rows in I are the same, and their difference are zero, leading to dark pixels in $|I - I'|$. When the 0^{th} dropped row occurs until the first (x_1), rows between the two images are different, leading to bright pixels in $|I - I'|$. After the first but before the second, the color transformation of the rows returns to normal; although the difference between pixel values in the two images is not zero, they are still pretty small, causing dark pixels in $|I - I'|$. So on, if we compute and visualize the difference between I' and I , it can be found that the bright regions correspond to the color strips in the reconstructed image.

Based on such an observation, we can use edge detection methods [36] to identify the positions of the color strips (i.e., x'_i) in I' . Because the dropped rows will shift the following rows up, it is essential to point out that the positions of the edges are not where the rows are dropped. It is not difficult to find the relationship between the edges and their corresponding dropped rows from Equation 1.

$$x_i = \begin{cases} x'_i, & \text{if } i = 0 \\ x'_i + 2 \times \lfloor \frac{i+1}{2} \rfloor, & \text{otherwise} \end{cases}$$

Therefore, we can obtain the dropped rows (D) in each image under attacks. Together with the raw image (I), the simulation method can be applied to generate simulated images (I^s).

V. EVALUATION OF SIMILARITY

As discussed in Section I, it is crucial to verify the equivalence of our simulation to real-world attacks. To accomplish this, our system model provides effective guidance through the following three aspects:

- I' v.s. I^s : Examining the similarity between raw images.
- $R(I')$ v.s. $R(I^s)$: Evaluating the similarity between reconstructed images.
- $C(R(I'))$ v.s. $C(R(I^s))$: Determining whether the reconstructed images have similar impacts on the computer vision algorithms.

A. Metrics

For the first two evaluations, we have chosen Structural Similarity Index Measure (SSIM) as the metric, which is widely used in image processing and computer vision to quantify the similarity between two images [37]. The last evaluation is about assessing the performance of computer vision tasks. We selected object detection for evaluation later because its susceptibility has been demonstrated in previous studies [12], [14], as well as a similar task, instance segmentation; these tasks are fundamental to other more advanced computer vision tasks [38]. The common metric for such tasks is Mean Average Precision (mAP) [39]. Below, we provided further details of these metrics.

1) *Structural Similarity Index Measure (SSIM)*: Assuming two images denoted by x and y , SSIM measures the similarity between them based on three main components: luminance, contrast, and structural similarity. The SSIM ranges from 0 to 1, where a value closer to 1 indicates a higher similarity between the images. It is calculated by:

$$\text{SSIM}(x, y) = \frac{(2\mu_x\mu_y + c_1) + (2\sigma_{xy} + c_2)}{(\mu_x^2 + \mu_y^2 + c_1)(\sigma_x^2 + \sigma_y^2 + c_2)}$$

where μ is the mean of pixels, and σ^2 is the variance, and c_1 and c_2 are variables to stabilize the division with weak denominator.

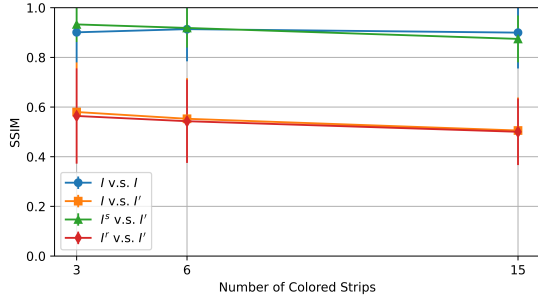


Fig. 7. SSIM between different raw images. The simulated adversarial images are highly similar to real attack images.

2) *Mean Average Precision (mAP)*: Precision and recall values are used to determine the average precision, where precision measures the accuracy of the detected objects (i.e., $p = \frac{\text{true_positive}}{\text{true_positive} + \text{false_positive}}$) and recall measures the completeness of the detection (i.e., $r = \frac{\text{true_positive}}{\text{true_positive} + \text{false_negative}}$). Average Precision (AP) is defined as:

$$AP = \sum_n (r_n - r_{n-1}) p_n$$

where r_n and p_n represent the n -th threshold, and AP can be simply regarded as the area under the precision-recall curve. The mAP score ranges from 0 to 1, with a higher value indicating a better performance. Note that there are different variants of mAP that will be used hereafter. For example, mAP50, mAP75, and mAP50:95 measure the mean average precision at an intersection over union (IoU) threshold of 0.5, 0.75, and across IoU thresholds ranging from 0.5 to 0.95, accordingly.

B. Structural Similarity between Raw Images

Firstly, we examined the SSIM between raw images unaffected by attacks. Note that two raw images are captured for each picture displayed on the monitor as mentioned in Section IV-B, and they can be used to calculate the SSIM. The average SSIM value is approximately 0.9, as depicted by “ I v.s. I ” in Figure 7. This value establishes a reference for the highest similarity between two images in our dataset. Note that when comparing the real attack image (I') to the non-attack image (I), the average SSIM drops to around 0.5, which is a reference for the lowest.

Next, we computed the SSIM between the real attack image (I') and the simulated adversarial image (I^s), resulting in an average SSIM as high as 0.9. This indicates that the simulated images closely resemble the real attack images at the raw image level. We also simulated a random drop of rows (represented as I'), where the dropped rows in the simulated image differ from those in the actual attack. The SSIM between I' and I^r is as low as 0.5, highlighting the superiority of our simulation method with accurately identifying dropped rows (detailed in Section IV-C) over a random approach. This further highlights the significant similarity achieved by our proposed simulation method.

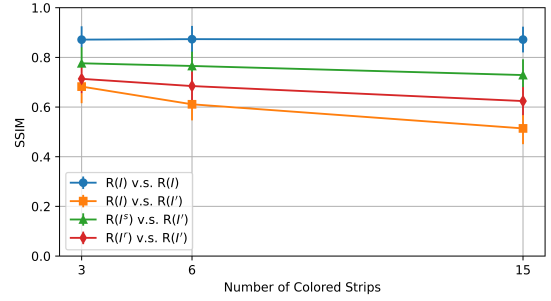


Fig. 8. SSIM between different reconstructed images. The simulated adversarial images are fairly similar to real attack images, where a drop from the high similarity in Figure 7 is attributed to noise amplified by the reconstruction process.

C. Structural Similarity between Reconstructed Images

Recalling the reconstruction process, which transforms a raw image into a complete image with full-color information, it can be complex and influenced by various factors such as demosaicing algorithms, white balancing, and noise reduction. Consequently, there exist numerous reconstruction functions. Note that the objective of this study is not to evaluate all reconstruction functions but rather to examine the similarity between reconstructed images, specifically $R(I')$ and $R(I^s)$. To approximate the reconstruction function $R(\cdot)$, we selected the widely used demosaicing algorithm, Adaptive Homogeneity-Directed Demosaicing Algorithm (AHD) [40].

Consistent with the previous subsection, we have considered four different reconstructed images: $R(I)$, $R(I')$, $R(I^s)$, and $R(I^r)$. We then calculated the SSIM for the following four comparison combinations, as illustrated in Figure 8.

As we can see, the highest similarity has been achieved by $R(I)$ v.s. $R(I)$ with average SSIM of 0.87, followed by $R(I^s)$ v.s. $R(I')$, and then $R(I^r)$ v.s. $R(I')$, and finally $R(I)$ v.s. $R(I')$ with the lowest similarity. From the results, the images reconstructed by using the real attack images and the images reconstructed by simulated adversarial images still displayed a similarity as high as 0.80, statistically significantly higher than the random simulation of 0.67.

It shows that our simulation method did manage to simulate the attack in a high resemblance, although not as close to the result before the reconstruction function. We attributed this discrepancy to the noise introduced by the attacks into the raw image. In Figure 5, the raw image under attacks (b) exhibits some noise compared to the original image (a) without attacks, albeit not prominently. However, after passing through the reconstruction functions, these noises are amplified and enhanced. Consequently, in (c), we have observed an increase in the presence of noise, manifested as colorful dots, which results in a lower SSIM between $R(I^s)$ v.s. $R(I')$, compared to the SSIM between I^s v.s. I' . Moreover, the more color strips, the more noisy the reconstructed image is, and hence, the SSIM between $R(I^s)$ v.s. $R(I')$ decreases while increasing the number of color strips.

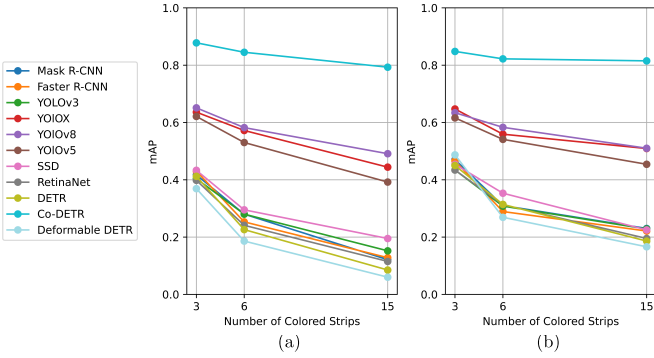


Fig. 9. Similar performance (mAP50) between (a) real attack images and (b) simulated adversarial images across different object detection models.

TABLE I
P-VALUES OF T-TEST REGARDING OBJECTION DETECTION.

	Number of Strips		
	3	6	15
mAP50	0.677	0.688	0.465
mAP75	0.998	0.682	0.569
mAP50:95	0.86	0.712	0.519

D. Performance Similarity

Our focus lies on assessing the performance of two computer vision tasks: object detection and instance segmentation, as mentioned previously. The objective is to evaluate the impact of both real and simulated adversarial images on these tasks, and demonstrate their comparable effects on different algorithms/models.

We began by employing the state-of-the-art models that have been benchmarked on the COCO dataset [35] to generate preliminary ground-truth labels for the tasks of object detection and image segmentation. Regarding object detection, we chose Co-DETR [41] which stands out as the current state-of-the-art model, while for instance segmentation, we chose Mask2Former [42]. These models provide an initial set of high-quality labels. Subsequently, we conducted a thorough manual review of these automatically generated labels. During this review, we adjusted and refined each label, which included correcting misclassified labels and fine-tuning the boundaries of the bounding boxes. This meticulous process ensures the accuracy of the labels used in our evaluation.

1) *Object Detection*: We carefully selected a diverse set of prominent models that highlight different strengths in object detection. For robust frameworks in object detection, we have chosen Mask R-CNN [43] and Faster R-CNN [44]. The YOLO [45] series (v3, v5, X, and v8) is chosen for its real-time processing capabilities, crucial for assessing performance under dynamic conditions. SSD [46] and RetinaNet [47] are included for their effectiveness in multi-scale detection and their innovative approaches to balancing class representation. Finally, the inclusion of DETR [48], Co-DETR [41], and Deformable DETR [49] allows us to explore the resilience of transformer-based models, which handle object relations differently than traditional convolutional approaches.

To evaluate the performance of these models on real attack images and simulated adversarial images, we calculated the

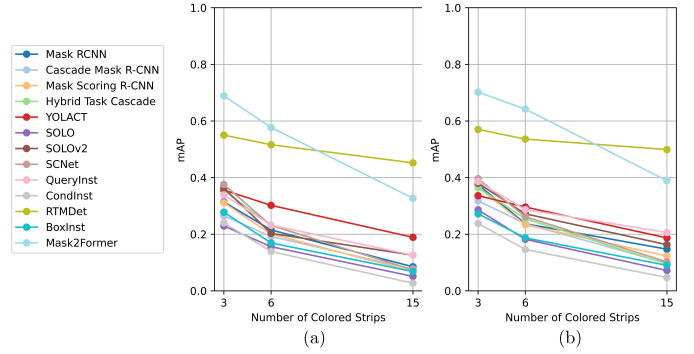


Fig. 10. Similar performance (mAP50) between (a) real attack images and (b) simulated adversarial images across different instance segmentation models.

TABLE II
P-VALUES OF T-TEST REGARDING INSTANCE SEGMENTATION.

	Number of Strips		
	3	6	15
mAP50	0.620	0.568	0.472
mAP75	0.601	0.531	0.601
mAP50:95	0.591	0.536	0.591

mean Average Precision (mAP). The mAP50 results are visualized in Figure 9, with (a) representing the performance on real attack images and (b) on simulated adversarial images. It is evident that as the number of color strips increases, the mAP values decrease. This consistent trend is observed in both real and simulated scenarios. Furthermore, to examine the null hypothesis that there is no significant statistical difference between the impacts of simulated and real attacks, we aggregated the mAP results across all selected models and conduct a t-test. We have chosen a commonly used significance level of 5%. The p-values from the t-test results for mAP50, mAP75, and mAP50:90 with different numbers of color strips are presented in Table I. As the p-values are larger than the significance level of 5%, we cannot reject the null hypothesis. Therefore, these results validate the effectiveness of simulated adversarial images in accurately replicating the effects of real attack images.

2) *Instance Segmentation*: We began by selecting a set of prominent models for instance segmentation. As classic methods for instance segmentation, Cascade Mask R-CNN [50] and Mask Scoring R-CNN [51] respectively introduce cascade structures and score predictors based on Mask R-CNN [43], providing robust frameworks for testing attack impact. Hybrid Task Cascade [52] fully leverages the information interaction between object detection and segmentation tasks, thereby improving overall performance. RTMDet [53] has chosen for evaluating attack impacts due to its excellent real-time processing capabilities in instance segmentation tasks. CondInst [54] and BoxInst [55] are also selected for their strong segmentation capabilities in occluded and dense scenes, respectively. Benefiting from the efficient handling of long sequence data by the attention mechanism, Mask2Former [42], SCNet [56], and QueryInst [57] effectively improves the accuracy and robustness of instance segmentation. Unlike most models that first perform object detection and then instance segmentation,

the SOLO models [58], [59] achieve efficient and precise instance segmentation by directly predicting the pixel-level positions.

Then, we applied these models to both real attack images and simulated adversarial images, and calculate mAP values. The results for mAP50 are visualized in Figure 10, with (a) depicting the models’ performance on real attack images, and (b) on the simulated adversarial images. Both plots show decreasing trends in the mAP as the number of color strips increases. To assess whether the performance on two types of images are similar, we aggregate the mAP across all selected models and analyze them via a t-test. The null hypothesis states that there is no significant statistical difference between the impacts of simulated and real attacks. Also, we select 5% as the significance level. In Table II, we present the p-values resulting from the t-test analysis for mAP50, mAP75, and mAP50:95, considering different numbers of color strips. It is not difficult to find that the p-values are much larger than 5%, and hence, we cannot reject the null hypothesis. In other words, these results further support the effectiveness of simulated adversarial images in accurately reflecting the effects of real attacks.

VI. CASE STUDY

In this section, we will demonstrate how to use our simulation method to explore the impacts of electromagnetic signal injection attacks on different models. Then, we will focus on enhancing the robustness of models against these attacks by leveraging the simulated adversarial images to fine-tune the models.

Note that we will use public datasets for the simulation. It is essential to point out that images in these datasets are not in the raw format. Therefore, we applied the state-of-the-art conversion tool, CycleISP [60], to obtain the raw format from RGB images, and then applied our simulation method to generate simulated adversarial images, with the number of strips ranging from 1 to 20, where their positions are random. Detailed discussion regarding the conversion process will be found in Section VII-A.

A. Susceptibilities of Different Models

1) *Models and Datasets*: In addition to object detection and instance segmentation, we have selected three more tasks, which are image classification, face recognition, and depth estimation, to evaluate the impact of attacks on computer vision tasks.

For the image classification task, we chose the highly-cited convolutional neural network architecture ResNet50 [61], the classic lightweight model Inception v3 [62], and a transformer-based model ViT [63]. To assess the performance of these three models, we measured their accuracy on the commonly used ILSVRC 2012 validation set [70].

For the face recognition task, we selected the classic models FaceNet [64], ArcFace [65], and the state-of-the-art model, AdaFace [66]. To evaluate their face recognition performance, we used the widely used IJB-C Face Dataset [71] and measured the 1:1 verification accuracy ($\text{TPR}@FPR=1e-4$) metric.

Note that this metric indicates the true positive rate of the models when performing a face-matching task with a false positive rate of $1e-4$, and the metric is commonly used in face recognition tasks above.

For the depth estimation task, we selected the classic model BTS [67]. Additionally, we considered the state-of-the-art transformer-based models DPT-Hybrid (also known as MiDaS) [68] and Depth Anything [69]. The SSIM metric is used to measure the similarity between the model’s output and the ground truth results on the classic KITTI dataset [72].

2) *Results and Analysis*: The results are presented in Table III. The performance of the models for each task is impacted when subjected to the “Attack” condition, as opposed to the “No Attack” condition. The degree of performance degradation, referred to as “Degradation” in the table, is measured as the percentage decrease in performance compared to the “No Attack” condition.

While almost all evaluated models experienced performance degradation under electromagnetic signal injection attacks compared to no-attack conditions, object detection and instance segmentation tasks proved more vulnerable. These tasks suffered a substantial performance drop up to 53%, in contrast to the more modest 16 - 31% decline observed in image classification, with Inception v3 showing the greatest resilience.

This pronounced disparity can be attributed to the inherent complexity of object detection and instance segmentation. Beyond classifying image content, these tasks demand precise localization and delineation of objects within the scene. Consequently, attacks possess a broader attack surface to manipulate image data, introducing errors in bounding box coordinates, and instance masks. Such manipulations can impact overall performance, as even minor inaccuracies in object localization can lead to cascading errors in subsequent processing stages.

In contrast to image classification, object detection, and instance segmentation, face recognition and depth estimation demonstrated greater resilience to electromagnetic signal injection attacks. While face recognition models experienced a decline in accuracy, the degradation was notably less severe compared to the other tasks. For instance, the state-of-the-art AdaFace model suffered only a 6% drop in performance. Depth estimation models exhibited exceptional robustness, with the leading Depth Anything model showing no discernible impact from the attacks. This suggests that these tasks might be less sensitive to the types of perturbations introduced by the electromagnetic signals. Potential reasons for this increased resilience could include the nature of the data processed (e.g., human faces, geometric information) and the specific algorithms employed in these models.

These findings highlight the vulnerability of different models and tasks to electromagnetic signal injection attacks, revealing significant variability in susceptibility across different tasks. Identifying the underlying reasons for performance degradation is crucial, as it could help and guide the development of effective defenses against such attacks. However, delving into these reasons is beyond the scope of this work. We acknowledge the importance of this investigation and consider it as a direction for future research.

TABLE III
SUSCEPTIBILITY OF DIFFERENT COMPUTER VISION TASKS TO ATTACKS

Tasks	Metric	Models	No Attack	Attack	Degradation
Image Classification	Accuracy	ResNet50 [61]	0.71	0.49	-31%
		Inception v3 [62]	0.68	0.57	-16%
		ViT [63]	0.70	0.55	-21%
Face Recognition	Accuracy	FaceNet [64]	0.45	0.35	-22%
		ArcFace [65]	0.84	0.77	-9%
		AdaFace [66]	0.87	0.81	-6%
Depth Estimation	SSIM	BTS [67]	0.93	0.91	-1%
		MiDaS [68]	0.93	0.92	-1%
		Depth Anything [69]	0.94	0.94	0%
Object Detection	mAP50	YOLOv8 [45]	0.70	0.57	-19%
		Mask R-CNN [43]	0.69	0.34	-51%
		DETR [48]	0.63	0.31	-51%
Instance Segmentation	mAP50	SOLOv2 [59]	0.53	0.27	-49%
		Mask R-CNN [43]	0.53	0.25	-53%
		RTMDet [53]	0.60	0.54	-10%

TABLE IV
PERFORMANCE OF DIFFERENT OBJECT DETECTION MODELS BEFORE/AFTER FINE-TUNING.

Model	Train	Validation	mAP50 (Degradation)	mAP75 (Degradation)	mAP50:95 (Degradation)
DETR [48]	-	No Attack	0.51	0.33	0.35
	-	Attack	0.25 (-50%)	0.16 (-52%)	0.16 (-55%)
	No Attack	Attack	0.21 (-59%)	0.14 (-59%)	0.13 (-63%)
	Attack	Attack	0.36 (-30%)	0.24 (-29%)	0.22 (-37%)
YOLOX [45]	-	No Attack	0.63	0.47	0.46
	-	Attack	0.52 (-17%)	0.37 (-22%)	0.37 (-20%)
	No Attack	Attack	0.46 (-27%)	0.36 (-23%)	0.33 (-27%)
	Attack	Attack	0.55 (-13%)	0.43 (-9%)	0.40 (-12%)
Faster R-CNN [44]	-	No Attack	0.55	0.39	0.36
	-	Attack	0.29 (-47%)	0.18 (-54%)	0.18 (-50%)
	No Attack	Attack	0.32 (-42%)	0.21 (-47%)	0.20 (-44%)
	Attack	Attack	0.34 (-37%)	0.22 (-43%)	0.22 (-39%)

B. Robustness Enhancement by Fine-tuning

In this section, we will demonstrate that fine-tuning models on Attack images can enhance their robustness against the attacks. We take object detection tasks as an example.

1) *Models and Datasets*: We pick three models: DETR [48], YOLOX [45], and Faster R-CNN [44]. These models are representatives of the transformer-based, one-stage, and two-stage families, respectively.

We randomly selected 1000 images from the COCO validation set for our experiments. These images are chosen to represent a diverse range of object categories and scenes, ensuring a comprehensive evaluation. The dataset is randomly split into training and validation subsets in a 70:30 ratio. This random split maintained the distribution of object categories across both subsets, and we ensured that the training set included all the labels present in the validation set.

To further demonstrate the effectiveness of fine-tuning on Attack images, we created two separate training sets. One set consisted of the original images (where there is no attack), while the other included images processed with Attacks. This setup allowed us to compare the improvements in robustness between models fine-tuned on non-attack images and those fine-tuned on images with simulated adversarial patterns. We trained all models on each training set for 150 epochs before

proceeding with validation, aiming to validate whether training on similar scenarios without attack patterns would yield as significant improvements as fine-tuning on images with simulated adversarial patterns.

Note that regarding the annotations for simulated adversarial images, it is crucial to account for the shifting effect as discussed in Section IV. Given an original annotated bounding box $[center_x, center_y, height, width]$, we must determine two factors: n_1 , the number of lines lost before $center_y$, and n_2 , the lines lost within the bounding box. The adjusted bounding box should be $[center_x, center_y - n_1, height - n_2, width]$ to ensure proper alignment with the simulated content. This adjustment maintains annotation integrity and ensures accurate reflection of the altered images.

2) *Results and Analysis*: The results are presented in Table VI-B. It can be found that models before fine-tuning show a significant drop in performance when validated on images with simulated adversarial patterns compared to those without attack patterns. For instance, DETR’s mAP50:95 drops from 0.35 to 0.16, and the degradation is 55%.

Fine-tuning the models solely on images without attack yielded minimal improvement in performance against adversarial attacks. In most cases (DETR and YOLOX), there was no significant enhancement in mAP when evaluated on

images with adversarial patterns compared to the non-fine-tuned models. This suggests that models trained on standard datasets might not inherently generalize well to adversarial settings.

In contrast, fine-tuning the models with images containing simulated adversarial patterns led to significant improvements in mAP across all models. DETR’s mAP50:95 increased from 0.16 to 0.22, indicating a reduction in performance degradation from 55% to 37%. This suggests that incorporating adversarial examples during fine-tuning equips the models to better recognize and handle these disruptions. Among the evaluated models, YOLOX exhibited the strongest baseline performance on clean images, with respect of different mAPs. Fine-tuning with adversarial images further enhanced YOLOX’s robustness against attacks. Its mAP50:95 increased to 0.40, retaining 88% ($= 1 - 12\%$) of its original performance under attack conditions. With respect to mAP75, up to 91% of the performance can be retained under attacks. Similarly, Faster R-CNN showed an increase in mAP50:95 from 0.18 to 0.22, mitigating the degradation from 50% to 39%.

Overall, fine-tuning the models on simulated adversarial images consistently improved model performance across all evaluated metrics, validating the approach of using such images to enhance robustness against adversarial attacks.

VII. DISCUSSION

A. Conversion from RGB to Raw

Referring back to Section VI, we employed a deep learning tool to convert RGB images into raw format, which were subsequently converted back to RGB using our simulation method. It is important to acknowledge that the conversion process from RGB to raw introduces degradation to the images, because this process involves estimating the values within the raw format (1 value/channel per pixel) from RGB format (3 values/channels per pixel), and this estimation inherently induces information loss. In terms of the impact on different computer vision tasks in Section VI-A, the degradation resulting from this conversion typically ranges from 5% to 20%. To avoid this degradation altogether, it is advisable to work with raw images captured directly by the camera, rather than resorting to the inverse conversion process.

VIII. RELATED WORK

While electromagnetic signal injection attacks have been discussed previously, we will not repeat them in this section. Instead, we concentrate on exploring the vulnerabilities and techniques associated with lights and acoustics, and we call these attacks as Light or Acoustic Signal Injection Attacks.

A. Light Signal Injection Attacks on Camera

Initially, these attacks focused on simply directing light towards the camera lens to blind automotive cameras. In 2015, Petit et al. [2] demonstrated the use of lasers to continuously blind automotive cameras, making them unable to detect objects. They also showed that rapidly switching the light on and off could confuse the camera’s auto controls, causing a

longer recovery and stabilization time for the image. Similarly, Yan et al. [3] revealed that directing a laser onto a camera could result in complete blindness for seconds, making image recognition impossible during that period. Fu et al. [4] further discussed the vulnerability of cameras and binocular vision sensors on drones to laser-based attacks.

Subsequently, researchers sought more precise control over the targeted systems. Wang et al. [5] exploited the features of infrared lights (IR lights) to manipulate the perception and mapping systems of autonomous vehicles (AVs). They discovered that IR lights, invisible to human eyes but detectable by AV cameras, could trigger image sensors and appear as magenta color in camera footage. This led to various attack scenarios, including generating invisible traffic lights, creating fake invisible objects, disrupting the in-car user experience, and introducing errors in the AV’s simultaneous localization and mapping (SLAM) process. Köhler et al. [6] explored the vulnerability of rolling shutter technology in cameras and its potential for exploitation. They demonstrated how a bright, modulated light source such as a low-cost laser could inject fine-grained disruptions into images captured by cameras, thereby concealing objects detected by state-of-the-art detectors. Additionally, Yan et al. [7] investigated the vulnerability of traffic light recognition systems to modulated laser interference. Man et al. [8] showcased how attackers could manipulate camera-based perception systems by projecting adversarial patterns into cameras, exploiting lens flare/ghost effects and auto-exposure control to create spurious objects or modify existing objects.

B. Acoustic Signal Injection Attacks on Camera

Ji et al. [9] and Cheng et al. [11] have identified a system-level vulnerability resulting from the combination of image stabilizer hardware, which is susceptible to acoustic manipulation, and computer vision algorithms that are vulnerable to adversarial examples. Through the emission of carefully designed acoustic signals, an attacker can manipulate the output of an inertial sensor, inducing unnecessary motion compensation and leading to blurred images even when the camera itself is stable. These blurred images can cause misclassification of objects and significantly impact critical decision-making processes in autonomous vehicles. Based on the vulnerability of the image stabilizer hardware in camera, Zhu et al. [11] present TPatch, a novel patch that remains benign under normal circumstances but can be triggered to initiate an attack when exposed to specific acoustic signals. By injecting acoustic signal attacks towards the cameras, the attacker can manipulate perception results, potentially resulting in dangerous driving decisions.

IX. CONCLUSION

In this work, we have addressed the emerging threat of electromagnetic signal injection attacks on camera-based smart systems. These attacks, which involve remotely injecting malicious electromagnetic signals into camera circuits, can manipulate captured images and lead to incorrect decisions by AI models. Our research filled the gaps in understanding

the vulnerability of camera-based smart systems to these attacks and developed effective solutions to mitigate the threat. To achieve these goals, we proposed a simulation method for generating manipulated images. This simulation method allows researchers and engineers to assess the vulnerability of computer vision applications without the need to construct complicated attack devices. To evaluate the effectiveness of our simulation method, we conducted a rigorous analysis comparing the simulated adversarial images with real-world manipulated images. Our results confirmed that the simulation closely resembles the effects of actual attack images. This validation provides confidence in the reliability and accuracy of our simulation approach. Through extensive experiments, we demonstrated that a significant majority of computer vision models are susceptible to electromagnetic signal injection attacks, highlighting the urgent need for robust defenses. Furthermore, we explored the potential mitigation strategy of adversarial training. By fine-tuning models with the simulation, we were able to enhance the robustness of different models against electromagnetic signal injection attacks. Our findings demonstrated a significant improvement, with up to 91% recovery in model performance. This promising result suggests that adversarial training could be a valuable direction for mitigating the impact of these attacks.

REFERENCES

- [1] A. Guesmi, M. A. Hanif, B. Ouni, and M. Shafique, "Physical Adversarial Attacks for Camera-based Smart Systems: Current Trends, Categorization, Applications, Research Challenges, and Future Outlook," *IEEE Access*, 2023.
- [2] J. Petit, B. Stottelaar, and M. Feiri, "Remote Attacks on Automated Vehicles Sensors: Experiments on Camera and LiDAR," 2015. [Online]. Available: <https://api.semanticscholar.org/CorpusID:39608826>
- [3] C. Yan, W. Xu, and J. Liu, "Can You Trust Autonomous Vehicles: Contactless Attacks against Sensors of Self-driving Vehicle," *Def Con*, vol. 24, no. 8, p. 109, 2016.
- [4] Z. Fu, Y. Zhi, S. Ji, and X. Sun, "Remote Attacks on Drones Vision Sensors: An Empirical Study," *IEEE Transactions on Dependable and Secure Computing*, vol. 19, no. 5, pp. 3125–3135, 2021.
- [5] W. Wang, Y. Yao, X. Liu, X. Li, P. Hao, and T. Zhu, "I Can See the Light: Attacks on Autonomous Vehicles Using Invisible Lights," in *Proceedings of the 2021 ACM SIGSAC Conference on Computer and Communications Security*, 2021, pp. 1930–1944.
- [6] S. Köhler, G. Lovisotto, S. Birnbach, R. Baker, and I. Martinovic, "They See Me Rollin': Inherent Vulnerability of the Rolling Shutter in CMOS Image Sensors," in *Proceedings of the 37th Annual Computer Security Applications Conference*, 2021, pp. 399–413.
- [7] C. Yan, Z. Xu, Z. Yin, S. Mangard, X. Ji, W. Xu, K. Zhao, Y. Zhou, T. Wang, G. Gu *et al.*, "Rolling Colors: Adversarial Laser Exploits against Traffic Light Recognition," in *31st USENIX Security Symposium (USENIX Security 22)*, 2022, pp. 1957–1974.
- [8] Y. Man, M. Li, and R. Gerdes, "Remote Perception Attacks against Camera-based Object Recognition Systems and Countermeasures," *ACM Transactions on Cyber-Physical Systems*, vol. 8, no. 2, pp. 1–27, 2024.
- [9] X. Ji, Y. Cheng, Y. Zhang, K. Wang, C. Yan, W. Xu, and K. Fu, "Poltergeist: Acoustic Adversarial Machine Learning against Cameras and Computer Vision," in *2021 IEEE Symposium on Security and Privacy (SP)*. IEEE, 2021, pp. 160–175.
- [10] Y. Cheng, X. Ji, W. Zhu, S. Zhang, K. Fu, and W. Xu, "Adversarial Computer Vision via Acoustic Manipulation of Camera Sensors," *IEEE Transactions on Dependable and Secure Computing*, 2023.
- [11] W. Zhu, X. Ji, Y. Cheng, S. Zhang, and W. Xu, "TPatch: A Triggered Physical Adversarial Patch," in *32nd USENIX Security Symposium (USENIX Security 23)*, 2023, pp. 661–678.
- [12] Q. Jiang, X. Ji, C. Yan, Z. Xie, H. Lou, and W. Xu, "GlitchHiker: Uncovering Vulnerabilities of Image Signal Transmission with IEMI," in *The 32nd USENIX Security Symposium*, 2023.
- [13] S. Köhler, R. Baker, and I. Martinovic, "Signal Injection Attacks against CCD Image Sensors," in *Proc. 2022 ACM ASIA Conference on Computer and Communications Security (ACM ASIACCS 2022)*. ACM, 2022.
- [14] Y. Zhang, C. Yang, Y. Fu, Q. Jiang, C. Yan, S.-Y. Chau, G. Ngai, H.-v. Leong, X. Luo, and W. Xu, "Understanding Impacts of Electromagnetic Signal Injection Attacks on Object Detection," in *IEEE International Conference on Multimedia and Expo*. IEEE, 2024.
- [15] M. G. Backstrom and K. G. Lovstrand, "Susceptibility of electronic systems to high-power microwaves: Summary of test experience," *IEEE Transactions on Electromagnetic Compatibility*, vol. 46, no. 3, pp. 396–403, 2004.
- [16] R. B. Schulz, "ELF and VLF Shielding Effectiveness of High-permeability Materials," *IEEE Transactions on Electromagnetic Compatibility*, no. 1, pp. 95–100, 1968.
- [17] P. F. Wilson, "Radiation Patterns of Unintentional Antennas: Estimates, Simulations, and Measurements," in *2010 Asia-Pacific International Symposium on Electromagnetic Compatibility*. IEEE, 2010, pp. 985–989.
- [18] C. R. Paul, R. C. Scully, and M. A. Steffka, *Introduction to Electromagnetic Compatibility*. John Wiley & Sons, 2022.
- [19] C. Yan, H. Shin, C. Bolton, W. Xu, Y. Kim, and K. Fu, "Sok: A Minimalist Approach to Formalizing Analog Sensor Security," in *2020 IEEE Symposium on Security and Privacy (SP)*. IEEE, 2020, pp. 233–248.
- [20] Y. Zhang, "Electromagnetic Signal Injection Attacks on Embedded Systems: Modeling and Detection," Ph.D. dissertation, University of Oxford, 2022.
- [21] D. F. Kune, J. Backes, S. S. Clark, D. Kramer, M. Reynolds, K. Fu, Y. Kim, and W. Xu, "Ghost Talk: Mitigating EMI Signal Injection Attacks against Analog Sensors," in *2013 IEEE Symposium on Security and Privacy*. IEEE, 2013, pp. 145–159.
- [22] X. Zhang, Y. Tu, Y. Long, L. Shan, M. A. Elsaadani, K. Fu, Z. Lin, and X. Hei, "From virtual touch to tesla command: Unlocking unauthenticated control chains from smart glasses for vehicle takeover," in *2024 IEEE Symposium on Security and Privacy (SP)*. IEEE Computer Society, 2024, pp. 201–201.
- [23] J.-H. Jang, M. Cho, J. Kim, D. Kim, and Y. Kim, "Paralyzing Drones via EMI Signal Injection on Sensory Communication Channels," in *NDSS*, 2023.
- [24] Y. Zhang and K. Rasmussen, "Electromagnetic Signal Injection Attacks on Differential Signaling," in *Proceedings of the 2023 ACM Asia Conference on Computer and Communications Security*, 2023, pp. 314–325.
- [25] J. Selvaraj, G. Y. Dayanıklı, N. P. Gaunkar, D. Ware, R. M. Gerdes, and M. Mina, "Electromagnetic Induction Attacks against Embedded Systems," in *Proceedings of the 2018 on Asia Conference on Computer and Communications Security*, 2018, pp. 499–510.
- [26] G. Y. Dayanıklı, A. Z. Mohammed, R. Gerdes, and M. Mina, "Wireless Manipulation of Serial Communication," in *Proceedings of the 2022 ACM on Asia Conference on Computer and Communications Security*, 2022, pp. 222–236.
- [27] Z. Xie, C. Yan, X. Ji, and W. Xu, "BitDance: Manipulating UART Serial Communication with IEMI," in *Proceedings of the 26th International Symposium on Research in Attacks, Intrusions and Defenses*, 2023, pp. 63–76.
- [28] S. Köhler, R. Baker, M. Strohmeier, and I. Martinovic, "Brokenwire: Wireless Disruption of CCS Electric Vehicle Charging," in *Proceedings 2023 Network and Distributed System Security Symposium*. Internet Society, 2023.
- [29] R. Szeliski, *Computer Vision: Algorithms and Applications*. Springer Nature, 2022.
- [30] A. Vouloudimos, N. Doulamis, A. Doulamis, and E. Protopapadakis, "Deep Learning for Computer Vision: A Brief Review," *Computational Intelligence and Neuroscience*, vol. 2018, no. 1, p. 7068349, 2018.
- [31] J. Chai, H. Zeng, A. Li, and E. W. Ngai, "Deep Learning in Computer Vision: A Critical Review of Emerging Techniques and Application Scenarios," *Machine Learning with Applications*, vol. 6, p. 100134, 2021.
- [32] B. Bayer, "Color Imaging Array," *United States Patent*, no. 3971065, 1976.
- [33] R. A. Maschal Jr, S. S. Young, J. Reynolds, K. Krapels, J. Fanning, and T. Corbin, "Review of Bayer Pattern Color Filter Array (CFA) Demosaicing with New Quality Assessment Algorithms," *Army Research Lab Adelphi Md Sensors and Electron Devices Directorate*, pp. 1–29, 2010.

- [34] Y. Long, Q. Jiang, C. Yan, T. Alam, X. Ji, W. Xu, and K. Fu, "EM Eye: Characterizing Electromagnetic Side-channel Eavesdropping on Embedded Cameras," *Proceedings of ACM NDSS*, 2024.
- [35] T.-Y. Lin, M. Maire, S. Belongie, J. Hays, P. Perona, D. Ramanan, P. Dollár, and C. L. Zitnick, "Microsoft COCO: Common Objects in Context," in *Computer Vision—ECCV 2014: 13th European Conference, Zurich, Switzerland, September 6–12, 2014, Proceedings, Part V 13*. Springer, 2014, pp. 740–755.
- [36] P. Virtanen, R. Gommers, T. E. Oliphant, M. Haberland, T. Reddy, D. Cournapeau, E. Burovski, P. Peterson, W. Weckesser, J. Bright, S. J. van der Walt, M. Brett, J. Wilson, K. J. Millman, N. Mayorov, A. R. J. Nelson, E. Jones, R. Kern, E. Larson, C. J. Carey, Í. Polat, Y. Feng, E. W. Moore, J. VanderPlas, D. Laxalde, J. Perktold, R. Cimrman, I. Henriksen, E. A. Quintero, C. R. Harris, A. M. Archibald, A. H. Ribeiro, F. Pedregosa, P. van Mulbregt, and SciPy 1.0 Contributors, "SciPy 1.0: Fundamental Algorithms for Scientific Computing in Python," *Nature Methods*, vol. 17, pp. 261–272, 2020.
- [37] Z. Wang, A. C. Bovik, H. R. Sheikh, and E. P. Simoncelli, "Image Quality Assessment: from Error Visibility to Structural Similarity," *IEEE transactions on image processing*, vol. 13, no. 4, pp. 600–612, 2004.
- [38] N. Manakitsa, G. S. Maraslidis, L. Moysis, and G. F. Fragulis, "A Review of Machine Learning and Deep Learning for Object Detection, Semantic Segmentation, and Human Action Recognition in Machine and Robotic Vision," *Technologies*, vol. 12, no. 2, p. 15, 2024.
- [39] R. Padilla, S. L. Netto, and E. A. Da Silva, "A Survey on Performance Metrics for Object-Detection Algorithms," in *2020 international conference on systems, signals and image processing (IWSSIP)*. IEEE, 2020, pp. 237–242.
- [40] K. Hirakawa and T. W. Parks, "Adaptive Homogeneity-directed Demosaicing Algorithm," *IEEE transactions on image processing*, vol. 14, no. 3, pp. 360–369, 2005.
- [41] Z. Zong, G. Song, and Y. Liu, "DETRs with Collaborative Hybrid Assignments Training," in *Proceedings of the IEEE/CVF International Conference on Computer Vision*, 2023, pp. 6748–6758.
- [42] B. Cheng, I. Misra, A. G. Schwing, A. Kirillov, and R. Girshick, "Masked-attention Mask Transformer for Universal Image Segmentation," 2022.
- [43] K. He, G. Gkioxari, P. Dollár, and R. Girshick, "Mask R-CNN," in *Proceedings of the IEEE International Conference on Computer Vision*, 2017, pp. 2961–2969.
- [44] R. Girshick, "Fast R-CNN," in *Proceedings of the IEEE International Conference on Computer Vision*, 2015, pp. 1440–1448.
- [45] J. Redmon, S. Divvala, R. Girshick, and A. Farhadi, "You Only Look Once: Unified, Real-Time Object Detection," in *Proceedings of the IEEE Conference on Computer Vision and Pattern Recognition*, 2016, pp. 779–788.
- [46] W. Liu, D. Anguelov, D. Erhan, C. Szegedy, S. Reed, C.-Y. Fu, and A. C. Berg, "SSD: Single Shot Multibox Detector," in *Computer Vision—ECCV 2016: 14th European Conference, Amsterdam, The Netherlands, October 11–14, 2016, Proceedings, Part I 14*. Springer, 2016, pp. 21–37.
- [47] T.-Y. Lin, P. Goyal, R. Girshick, K. He, and P. Dollár, "Focal Loss for Dense Object Detection," in *Proceedings of the IEEE International Conference on Computer Vision*, 2017, pp. 2980–2988.
- [48] N. Carion, F. Massa, G. Synnaeve, N. Usunier, A. Kirillov, and S. Zagoruyko, "End-to-end Object Detection with Transformers," in *European conference on computer vision*. Springer, 2020, pp. 213–229.
- [49] X. Zhu, W. Su, L. Lu, B. Li, X. Wang, and J. Dai, "Deformable {DETR}: Deformable Transformers for End-to-End Object Detection," in *International Conference on Learning Representations*, 2021. [Online]. Available: <https://openreview.net/forum?id=gZ9hCDWe6ke>
- [50] Z. Cai and N. Vasconcelos, "Cascade R-CNN: High Quality Object Detection and Instance Segmentation," *IEEE transactions on Pattern Analysis and Machine Intelligence*, vol. 43, no. 5, pp. 1483–1498, 2019.
- [51] Z. Huang, L. Huang, Y. Gong, C. Huang, and X. Wang, "Mask Scoring R-CNN," in *Proceedings of the IEEE/CVF Conference on Computer Vision and Pattern Recognition*, 2019, pp. 6409–6418.
- [52] K. Chen, J. Pang, J. Wang, Y. Xiong, X. Li, S. Sun, W. Feng, Z. Liu, J. Shi, W. Ouyang *et al.*, "Hybrid Task Cascade for Instance Segmentation," in *Proceedings of the IEEE/CVF Conference on Computer Vision and Pattern Recognition*, 2019, pp. 4974–4983.
- [53] C. Lyu, W. Zhang, H. Huang, Y. Zhou, Y. Wang, Y. Liu, S. Zhang, and K. Chen, "RTMDet: An Empirical Study of Designing Real-Time Object Detectors," *arXiv preprint arXiv:2212.07784*, 2022.
- [54] Z. Tian, C. Shen, and H. Chen, "Conditional Convolutions for Instance Segmentation," in *Computer Vision—ECCV 2020: 16th European Conference, Glasgow, UK, August 23–28, 2020, Proceedings, Part I 16*. Springer, 2020, pp. 282–298.
- [55] Z. Tian, C. Shen, X. Wang, and H. Chen, "BoxInst: High-Performance Instance Segmentation with Box Annotations," in *Proceedings of the IEEE/CVF Conference on Computer Vision and Pattern Recognition*, 2021, pp. 5443–5452.
- [56] T. Vu, H. Kang, and C. D. Yoo, "Scnet: Training inference sample consistency for instance segmentation," in *Proceedings of the AAAI Conference on Artificial Intelligence*, vol. 35, no. 3, 2021, pp. 2701–2709.
- [57] Y. Fang, S. Yang, X. Wang, Y. Li, C. Fang, Y. Shan, B. Feng, and W. Liu, "Instances as Queries," in *Proceedings of the IEEE/CVF International Conference on Computer Vision*, 2021, pp. 6910–6919.
- [58] X. Wang, T. Kong, C. Shen, Y. Jiang, and L. Li, "SOLO: Segmenting Objects by Locations," in *Computer Vision—ECCV 2020: 16th European Conference, Glasgow, UK, August 23–28, 2020, Proceedings, Part XVIII 16*. Springer, 2020, pp. 649–665.
- [59] X. Wang, R. Zhang, T. Kong, L. Li, and C. Shen, "SOLOv2: Dynamic and Fast Instance Segmentation," *Advances in Neural information processing systems*, vol. 33, pp. 17 721–17 732, 2020.
- [60] S. W. Zamir, A. Arora, S. Khan, M. Hayat, F. S. Khan, M.-H. Yang, and L. Shao, "CycleISP: Real Image Restoration via Improved Data Synthesis," in *Proceedings of the IEEE/CVF Conference on Computer Vision and Pattern Recognition*, 2020, pp. 2696–2705.
- [61] K. He, X. Zhang, S. Ren, and J. Sun, "Deep Residual Learning for Image Recognition," in *Proceedings of the IEEE Conference on Computer Vision and Pattern Recognition*, 2016, pp. 770–778.
- [62] C. Szegedy, V. Vanhoucke, S. Ioffe, J. Shlens, and Z. Wojna, "Rethinking the Inception Architecture for Computer Vision," in *Proceedings of the IEEE Conference on Computer Vision and Pattern Recognition*, 2016, pp. 2818–2826.
- [63] A. Dosovitskiy, L. Beyer, A. Kolesnikov, D. Weissenborn, X. Zhai, T. Unterthiner, M. Dehghani, M. Minderer, G. Heigold, S. Gelly *et al.*, "An Image is Worth 16x16 Words: Transformers for Image Recognition at Scale," *arXiv preprint arXiv:2010.11929*, 2020.
- [64] F. Schroff, D. Kalenichenko, and J. Philbin, "FaceNet: A Unified Embedding for Face Recognition and Clustering," in *Proceedings of the IEEE Conference on Computer Vision and Pattern Recognition*, 2015, pp. 815–823.
- [65] J. Deng, J. Guo, X. Niannan, and S. Zafeiriou, "ArcFace: Additive Angular Margin Loss for Deep Face Recognition," in *CVPR*, 2019.
- [66] M. Kim, A. K. Jain, and X. Liu, "AdaFace: Quality Adaptive Margin for Face Recognition," in *Proceedings of the IEEE/CVF Conference on Computer Vision and Pattern Recognition*, 2022.
- [67] J. H. Lee, M.-K. Han, D. W. Ko, and I. H. Suh, "From Big to Small: Multi-scale Local Planar Guidance for Monocular Depth Estimation," *arXiv preprint arXiv:1907.10326*, 2019.
- [68] R. Ranftl, A. Bochkovskiy, and V. Koltun, "Vision Transformers for Dense Prediction," *ArXiv preprint*, 2021.
- [69] L. Yang, B. Kang, Z. Huang, X. Xu, J. Feng, and H. Zhao, "Depth Anything: Unleashing the Power of Large-Scale Unlabeled Data," in *CVPR*, 2024.
- [70] O. Russakovsky, J. Deng, H. Su, J. Krause, S. Satheesh, S. Ma, Z. Huang, A. Karpathy, A. Khosla, M. Bernstein, A. C. Berg, and L. Fei-Fei, "ImageNet Large Scale Visual Recognition Challenge," *International Journal of Computer Vision (IJCV)*, vol. 115, no. 3, pp. 211–252, 2015.
- [71] B. Mazi, J. Adams, J. A. Duncan, N. Kalka, T. Miller, C. Otto, A. K. Jain, W. T. Niggel, J. Anderson, J. Cheney, and P. Grother, "IARPA Janus Benchmark - C: Face Dataset and Protocol," in *2018 International Conference on Biometrics (ICB)*, 2018, pp. 158–165.
- [72] A. Geiger, P. Lenz, and R. Urtasun, "Are We Ready for Autonomous Driving? The KITTI Vision Benchmark Suite," in *Conference on Computer Vision and Pattern Recognition (CVPR)*, 2012.